arXiv:astro-ph/9601152v1 26 Jan 1996

submitted to Astrophysical Journal

Probing Lyα Absorbers in Cosmological Simulations with Double Lines of Sight

Jane C. Charlton[1]
Astronomy and Astrophysics Department
Pennsylvania State University
University Park, PA 16802
charlton@astro.psu.edu

and

Peter Anninos, Yu Zhang[2] and Michael L. Norman[2]
Laboratory for Computational Astrophysics
National Center for Supercomputing Applications
University of Illinois at Urbana-Champaign
405 N. Matthews Ave., Urbana, IL 61801
panninos, yzhang, norman@ncsa.uiuc.edu

ABSTRACT

We perform a double line of sight (DLOS) analysis of the Lyα forest structures that form and evolve in cosmological N–body/hydrodynamic simulations. Pairs of simulated spectra, extracted from lines of sight separated by distances from $D = 12.5$ kpc up to 800 kpc, and a "control sample" of unrelated lines of sight, are analyzed at redshifts 3, 2, and 1. Coincident line samples are defined for HI column density thresholds $N_{co} = 10^{12.5}$, 10^{13}, and 10^{14} cm^{-2}. We find that: 1) Under the assumption of a single structure size, a Bayesian analysis yields sizes that are larger for smaller N_{co}, and at fixed N_{co} the size decreases with decreasing redshift. However, these derived sizes are found to increase with increasing D indicating that the assumption of a single structure size is invalid. 2) The column densities of coincident pairs are highly correlated for small D, with increasing scatter as D is increased, consistent with structures that have a centrally peaked N_H that decreases gradually with radius. 3) The velocity difference distribution for coincident lines is very narrow for small D, and widens as D is increased to meet the expectation for chance coincidences in unrelated lines of sight. This behavior is indicative of organized motion within the structures. 4) For small D, the distribution of anticoincident line column densities, N_{ac}, falls steeply as N_{ac} increases from the cutoff

[1]Center for Gravitational Physics and Geometry, Pennsylvania State University

[2]Astronomy Department, University of Illinois

value, but has a significant tail at large values which is inconsistent with a population of spherical absorbers with sharp edges, and consistent with a flattened geometry. The conclusions reached on the basis of the DLOS analysis are validated by an examination of the three–dimensional structures and velocity flows in the simulation data.

Subject headings: quasars: absorption lines — galaxies: structure — galaxies: evolution

1. Introduction

Observations of the spectra of double line of sight (DLOS) quasars are the most promising method for determining the sizes and distribution of material in the Lyα absorbing structures and for studying their evolution over time. Analysis based on present observations is limited by the number of close quasar pairs that are bright enough to obtain spectra at high resolution, but this situation will be rectified as new quasars are discovered. Numerical cosmological simulations have been quite successful in matching the properties of observed structures, even down to the scale of the Lyα forest (Cen *et al.* 1994, Zhang, Anninos, & Norman 1995, Hernquist *et al.* 1996, Miralda–Escudé *et al.* 1996). In this paper we use the results of these simulations as a laboratory in which to conduct DLOS analysis. The objectives of this study are to obtain a more intuitive understanding of the formation and evolution of structure in the simulations themselves and to aid interpretation of more detailed DLOS analysis tools in view of the promise of abundant new data.

Existing DLOS observations demonstrate that the structures responsible for Lyα forest absorption lines are much larger than predicted by standard CDM mini-halo (Rees 1986, Miralda–Escudé & Rees 1993) or pressure confined (Sargent *et al.* 1980, Ikeuchi & Ostriker 1986) models. The strongest constraint at redshift ~ 2 comes from the separation $\sim 40\ h^{-1}$ kpc DLOS Q1343+266 A,B (Bechtold 1994, Dinshaw *et al.* 1994). A Bayesian statistical analysis of the number of coincident and anticoincident lines in these spectra yielded a median radius (in the probability distribution) of 149 h^{-1} kpc and a 99% confidence lower limit of $R = 61\ h^{-1}$ kpc (for $\Omega_0 = 1$ where $h = H_0/100$ km s^{-1} Mpc^{-1}) (Fang *et al.* 1996). At the lower median redshift of 0.7, analysis of the separation $\sim 330\ h^{-1}$ kpc DLOS Q0107-0232/0235 (Dinshaw *et al.* 1995) gives an even larger median radius of 501 h^{-1} kpc (Fang *et al.* 1996) under the assumption of a single population of spherical clouds. However, analysis of several additional widely separated pairs (Fang *et al.* 1996) yields a trend for an increasing derived cloud radius with increasing DLOS separation, even at a fixed redshift, calling into question the simple single population assumption. Fang *et al.* (1995) suggest that a distribution of sizes and/or correlated (but smaller) structures could be more consistent. Additional data on DLOS pairs at various separations and for lines with different column density cutoffs will be important to determine the evolution of structure sizes.

Observations of very close QSO pairs (less than tens of kpc) show nearly identical equivalent widths and redshifts for common lines (Smette *et al.* 1992, Smette *et al.* 1995, Bechtold & Yee

1996). There is some evidence that the radial velocity difference distribution for coincident lines widens with increasing DLOS separation, and that the equivalent widths deviate more from the correlation line (Dinshaw *et al.* 1994, Fang *et al.* 1996). These trends would result from structures with column densities that peak towards the center and smoothly decrease with radius, and in which some type of coherent velocity structure is also present (Charlton, Churchill, & Linder 1995; hereafter CCL95). Such structures are like what one would expect for outer extensions of galaxies, and in fact at low redshifts many Lyα forest lines appear to result from these regions (Lanzetta *et al.* 1995).

Here we will perform a detailed DLOS analysis of the results from two different numerical simulations (box sizes 3.2 and 9.6Mpc) using our hierarchical N–body/hydrodynamics code (HERCULES) (Anninos, Norman, & Clarke 1994, Anninos *et al.* 1996). Our DLOS analysis will include a Bayesian analysis of structure sizes, and an application of the tests developed in CCL95. That paper presented the expected distributions of coincident and anticoincident line properties for "toy" models in spherical and disk geometries. Three diagnostic tests for geometry and for the distribution of mass within structures were applied: 1) comparison of neutral Hydrogen column densities N_H for lines coincident in the two lines of sight; 2) distributions of the differences in velocities between coincident lines; 3) the distribution of N_H for anticoincident lines. Application of these tests to the limited existing data at redshift two (weighted heavily by consideration of DLOS Q1343+266 A,B) led to the conclusion that slab/disk–like, smooth structures with $N_H \sim R^{-4}$ and with coherent internal motion (such as rotation or inflow) are consistent.

In the study of the Lyα forest, the relationship between numerical simulation data and observational data is symbiotic. By performing DLOS analysis on numerical simulations we gain the ability to probe all different separations over the full range of redshifts. This enables a diagnosis of the nature of the Lyα structures produced by the simulations and an exploration of their evolution. The results of this DLOS analysis will be compared to those from similar analysis of existing observational data. Finally, the simulation data have the distinct advantage of providing complete knowledge of the distribution of matter in space, velocity, and time. This provides a check on intuitions developed purely on the basis of DLOS analysis, and allows further development of tools that can be used both for simulations and for observational data.

This paper begins in §2 with a summary of our numerical techniques and methods used to generate and analyze simulated spectra. Section 3 presents the results of the various DLOS tests, including a Bayesian size analysis, column density distributions of coincident lines, velocity differences of coincident lines, and column density distributions of anticoincident lines. We conclude with a discussion in §4 of the various lessons learned from the analysis of simulation data.

2. Numerical Methods

The cosmological simulations discussed in this paper were conducted using the three-dimensional hierarchical code (HERCULES) that we have developed to solve the N-body equations for the dark matter particles, the hydrodynamic equations for the baryonic gas, and the cosmological expansion equation for the FLRW background universe. The code also models the radiative cooling of the gas, supplies an external flux of ionizing radiation, and solves the non-equilibrium rate equations for 27 chemical reactions involving nine atomic and molecular species (including the various ions of Hydrogen and Helium). Further details and tests of this code can be found in Anninos, Norman & Clarke (1994) and Anninos *et al.* (1996).

We have performed two simulations using different box sizes with comoving dimensions 3.2 Mpc and 9.6 Mpc. The smaller 3.2 Mpc box calculation is initialized with a cold dark matter (CDM) fluctuation spectrum normalized to $\sigma_8 = 1$, with a Hubble constant $H_0 = 70$ km s^{-1} Mpc^{-1}, total density parameter $\Omega_0 = 1$, and baryon fraction $\Omega_B = 0.04$. The baryonic component is composed of Hydrogen and Helium in cosmic abundance with a Hydrogen mass fraction of 76%. A photoionizing radiation field with spectral index $\alpha = 1.5$ is turned on at $z = 6.5$ and increased in redshift to a maximum value of $J_{912} = 8 \times 10^{-23}$ ergs s^{-1} cm^{-2} Hz^{-1} sr^{-1} at $z = 4.5$, held constant until $z = 0.5$, then decreased linearly with redshift to 10% of J_{912} at $z = 0$. The parameters of the larger 9.6 Mpc box calculation are similarly defined except that a second year COBE normalization of the CDM fluctuations is used with $\sigma_8 = 1.36$. Also, for the large box simulation we set $H_0 = 50$ km s^{-1} Mpc^{-1} and $\Omega_B = 0.06$. The radiation is increased with redshift from $z = 6.5$ to a larger amplitude (than the 3.2 Mpc case) $J_{912} = 2 \times 10^{-22}$ ergs s^{-1} cm^{-2} Hz^{-1} sr^{-1} at $z = 4.5$, held constant, then decreased linearly from $z = 2$ to 10% of J_{912} at $z = 0$.

Taken together, the two simulations allow us to simultaneously explore the effect of varying the physical parameters, grid resolution, and large scale gravitational tidal fields. In particular we note that the larger box simulation has a cell size of only $\Delta x = 19$ kpc at $z = 3$ (and a factor of two worse at $z = 1$), and therefore will not be of value for comparisons of close lines of sight. The small box simulation has a resolution of 6.3 kpc at $z = 3$, and thus we can consider DLOS with separations 25 kpc, and with some caution, even 12.5 kpc. In order to best examine the formation and clustering of structures (that can be several hundred kpcs in size) it is important to consider the effect of the surrounding environment and the distribution of matter on large scales, thus the large box simulation is complementary to the small box simulation which has higher resolution and greater ability to resolve cooling flows.

We have performed a DLOS analysis on the results of both the 3.2 Mpc and 9.6 Mpc box simulations. Spectra were generated for various random lines of sight through the simulation boxes using a convolution procedure (Bi *et al.* 1995, Zhang, Anninos, & Norman 1996). The optical depth is computed at each point in velocity space by integrating $\tau = c \int n_H \sigma dt$ (where n_H is the number density of neutral Hydrogen, c is the speed of light, dt is the interval of time, and σ is the absorption cross section assuming a Voigt profile for the lines) along a LOS from the QSO source. The total

velocity for an absorption feature is the combination of the Hubble flow velocity and the peculiar velocity, which is computed from the local gravitational acceleration, pressure gradient forces, and bulk fluid motion for each contributing cell. The transmission along the line of sight is then given by $e^{-\tau}$.

A series of parallel lines of sight for the 3.2 Mpc box at $z = 2$ are shown in Fig. 1. Qualitatively, the two spectra are nearly identical (both in the presence of lines coincident in redshift and in the strengths of these lines) for small separations, begin to differ substantially as the DLOS separation increases, but still exhibit similarities even on the scale of hundreds of kpc. The spectra also appear similar over different redshift ranges except that the opacities become smaller with decreasing redshift at a rate that depends on the cosmological expansion, the ionizing radiation flux, and the density of lines. The density of lines itself decreases along the DLOS with decreasing redshift, in agreement with observations (Lu, Wolfe, & Turnshek 1991, Bechtold 1994, Bahcall *et al.* 1996).

To facilitate a quantitative analysis of the DLOS we must identify and extract individual lines from the spectra. Absorption features are identified as locations in the spectra where the opacity is greater than some pre–determined critical value, typically 0.2. A second selection procedure is then applied to identify individual lines as those features which have a clear central maximum opacity. These lines are then fit with Gaussian profiles, allowing for multiple profiles to provide adequate fits to saturated and/or blended features. The Doppler parameters and column densities of the extracted lines are computed from the line center opacity, the equivalent width $W_\lambda = \int (1 - e^{-\tau})\, d\lambda$, and the curve of growth for a Maxwellian velocity distribution (Spitzer 1978). Further details of this procedure are provided in Zhang *et al.* (1996).

For each of three redshifts ($z = 3$, 2, and 1) and two box sizes ($L = 3.2$ and 9.6 Mpc), and for seven DLOS separations ($D = 12.5$, 25, 50, 100, 200, 400, and 800 kpc), we produce 1000 pairs of parallel spectra, each extending over a redshift interval $\Delta z = 0.1$. In the remainder of this paper, we will focus on what can be learned from the DLOS analysis of these simulated data.

3. Double Line of Sight Analysis

In analyses of observational data, the sizes of Lyα absorbing structures were estimated by using the numbers of "coincident" and "anticoincident" lines in DLOS (Dinshaw *et al.* 1994, Bechtold 1994, Dinshaw *et al.* 1995, Fang *et al.* 1996). A coincidence was defined as a case where lines were present in both lines of sight above some S/N threshold and within a velocity interval of $\Delta V < 150$ km/s. An anti-coincidence was defined as a case of a line in one LOS without a detected line in the other LOS within $\Delta V < 150$ km/s. In the rare case that two lines in one line of sight fall within 150 km/s of a line in the other line of sight, Fang *et al.* (1995) counted only one coincidence, but also did not include the third line as an anticoincidence. For the equivalent width detection thresholds of these spectra (using ≤ 4 m telescopes) the probability of coincidences occurring by chance is minimal. However, for more abundant weaker lines (as in these simulated data or in

forthcoming 8–m class telescope spectra) and/or at high redshift this will no longer be the case.

In view of the difficulties of correcting for random coincidences, we adopt the following simplest procedure for defining coincident pairs. For each line in one LOS we define a coincidence with the closest line in velocity along the other LOS if this line is within our coincidence velocity criterion ΔV_{co} (either 150 km/s or 50 km/s). An anticoincidence is counted only if there is no line within ΔV_{co} in the other LOS. This leaves us with another set of lines that are within ΔV_{co} of another line, but are not the closest in velocity space, which we shall call adjacent lines.

For each redshift and box size, and for two choices of ΔV_{co} we analyze separately the set of lines exceeding column density thresholds $N_{co} = 10^{12.5}$, 10^{13}, and 10^{14} cm^{-2}. Fig. 2 displays for the 3.2 Mpc box simulation (solid curves) the ratio of the number of coincidences to the sum of the number of coincidences and anticoincidences, f_{co}, as a function of the DLOS separation. The fraction of coincidences generally decreases with increasing D, but levels off at large D. The slow flattening of these curves at large separations is attributed to chance coincidences. For $\Delta V_{co} =$ 150km/s, nearly all lines are coincident if $z \geq 2$ and/or $N_H \leq 10^{13}$ cm^{-2} The more restrictive cutoff, $\Delta V_{co} = 50$ km/s, is generally more useful for our analysis.

To consider the effect of chance coincidences on DLOS analyses we construct "control samples" of unrelated lines of sight. This is accomplished by dividing each of the 1000 lines of sight (for a given redshift and box size) at the midpoint into two equal parts and analyzing each of these pairs as if it was a DLOS. The fractions of coincident lines to arise in these "control samples", for the three N_{co} values in the 3.2 Mpc box, are given as solid horizontal lines in Fig. 2. The fraction of chance coincidences becomes comparable to the fraction of coincidences for real DLOS at large D, but there is an "excess" of real coincidences at small D in all cases. Clearly, chance coincidences make a significant contribution for large z and small N_{co}.

The dashed curves and horizontal lines in Fig. 2 give a comparison for $N_{co} = 10^{12.5}$ cm^{-2} in the 9.6 Mpc box simulation. Several effects compete to determine the effect of the box size on f_{co}. The 9.6 Mpc box has a more realistic representation of large scale structure, and a larger cell size, which together act to increase f_{co} over both large and small D. However, because of the higher spatial resolution in the 3.2 Mpc box, the density of lines along the spectrum is greater than in the larger box. The smaller box thus has a larger fraction of chance coincidences (compare the dashed and the upper solid lines), which increases f_{co} at large D. This latter effect dominates for $z \geq 2$, so that the 3.2 Mpc box simulations have larger f_{co}. For the cases with $z = 1$, the levels of chance coincidences in both the 3.2 Mpc and in the 9.6 Mpc simulations are small compared to f_{co}, particularly at small D, and the effect of large scale power in the larger box leads to a larger f_{co}.

It is not straight–forward to correct for the effect of chance coincidences, but we can estimate their relative importance. Subtracting the estimated number of chance coincidences leads to overcorrection: in cases with large f_{co} it is clear that many of the coincidences are indicative of real structures so that the actual number of chance coincidences is much smaller than the number derived from unrelated LOS. As an example, consider a sample of all lines with neutral column

density $N_H > 10^{12.5}$ cm^{-2}. For the small box simulation at $z = 2$, with the largest DLOS separation of $D = 800$ kpc, and with $\Delta V_{co} = 150$ km/s, in our 1000 DLOS there are 45200 coincidences, 13644 anticoincidences, and 13877 adjacent lines. If we are more restrictive, with $\Delta V_{co} = 50$ km/s, the number of coincidences is reduced to 24393, the number of anticoincidences increases to 55379, and the number of adjacent lines decreased to only 3313 (3% of the total number of lines). If all coincidences were by chance, since the fraction of the lines in one LOS that are coincident is 0.45 we would expect a fraction $(0.45)^2$, or 20% of the lines to be adjacent. The small observed number of adjacent lines is indicative that a significant number of the coincidences are real, even at large D. In the following analysis we will not attempt to quantitatively "correct" for chance coincidences, but will refer to Fig. 2 to assess the implications of this effect.

3.1. Maximum Likelihood Sizes

With the simplified assumption that the structures responsible for Lyα absorption (above a given N_{co}) are a single population of uniform size we can apply Bayesian statistics to estimate the structure sizes at the various N_H contour levels. We follow the procedure given in Fang *et al.* (1995), using the numbers of coincidences (or "hits" $\mathcal{N}_h$) and anticoincidences (or "misses" $\mathcal{N}_m$) to evaluate the probability $P(R)$ that the radius of the single population has value R, for a spherical and for a disk geometry. As in Fang *et al.* (1995), we define $X = D/2R$ so that the probabilities, for the two geometries, that a second LOS intersects the structure if a first one does are:

$$\phi_{sphere} = \frac{2}{\pi}\left[\cos^{-1} X - X(1-X^2)^{1/2}\right] \qquad \text{for} \quad X < 1 \ ,$$

$$\phi_{disk} = \int_{-\pi/2}^{\pi/2} \frac{\cos\theta}{\pi}\left[\cos^{-1}\left(\frac{X}{\cos\theta}\right) - \frac{X}{\cos\theta}\left(1 - \frac{X^2}{\cos^2\theta}\right)^{1/2}\right] d\theta \qquad \text{for} \quad X < \cos\theta \ ,$$

and 0 otherwise. Defining the related quantity, $\psi = \phi/(2-\phi)$, the probability that both LOS intersect the structure, knowing that at least one of them does, we can calculate the maximum likelihood probability that the structure has radius R as

$$P(R) = \frac{(\mathcal{N}_h + \mathcal{N}_m + 1)!}{\mathcal{N}_h!\mathcal{N}_m!}\psi^{\mathcal{N}_h}(1-\psi)^{\mathcal{N}_m}\frac{d\psi}{dR}$$

where

$$\frac{d\psi}{dR} = \frac{8}{\pi}\frac{X}{R}(1-X^2)^{1/2}(2-\phi)^{-2}.$$

Fang *et al.* "correct" for random coincidences by subtracting the number of chance pairs expected (aside from those that would be classified as adjacent lines) from the observed number and by adding twice this number to the number of anticoincidences. This procedure works well in cases where the density of lines is low (high N_H threshold or low z), but it is not sufficient if the number of accidental hits is comparable to the number of coincidences even for very close lines of sight. For our

analysis, we simply used the observed number of coincidences and anticoincidences, disregarding adjacent lines, and acknowledging that the resulting sizes will be overestimated, particularly for large DLOS separations.

Figure 3 presents the median sizes from $P(R)$ derived from the Bayesian analysis of various sets of the simulated spectra as a function of DLOS separation. If the assumption of a single, uncorrelated population of structures is valid and if contamination by chance coincidences is insignificant, we expect the size derived to be constant at various DLOS separations. Yet we see that for all curves the derived size increases with increasing D. Each panel of Fig. 3 gives three curves, corresponding to $z = 3$, 2, and 1, and the series on the top shows the median sizes at the three contour levels $10^{12.5}$, 10^{13}, and 10^{14} cm^{-2} derived with the criterion $\Delta V < 50$ km/s for coincident lines (for the large 9.6 Mpc box simulation). Smaller sizes result from the assumption of a spherical cloud population, as illustrated by a comparison of Figs. 3a and 3d. The effect of the box size/resolution is illustrated by a comparison of the median radii for 10^{13} cm^{-2} contour levels in Figs. 3b (9.6 Mpc box) and 3e (3.2 Mpc box). For this case, derived sizes are somewhat larger in the 9.6 Mpc box, because the effect of enhanced power on larger scales dominates over the effect of a larger chance pair contribution in the small box. Finally, the effect of relaxing the ΔV criterion to 150 km/s is shown in Fig. 3f for the 10^{14} cm^{-2} contour. This less restrictive criterion can add more "real" coincidences as well as more accidental ones, but at large D most of the increase of the derived median size is likely to be due to the added contamination.

The assumption of single sized structures is only an approximation, but it is still useful to give rough numbers for the sizes of structures at the different N_{co} and z. The most reliable size estimate will come from an intermediate D range (roughly comparable to the structure size). Smaller D estimates are suspect due to the low resolution of the simulations on these scales, while at larger D the chance pairs make a larger contribution to the measured number of coincidences. The median size does not change too rapidly in the regime where $D \sim R$. We derive the rough numbers from the large box simulations because of the more realistic handling of large scale power, and because of the lesser contamination by chance coincidences (due to the smaller line density). Ultimately, a better method is needed to quantify the size for cases with a high density of lines.

The following basic results for sizes and size evolution can be extracted from the simulation data: 1) At all redshifts we find that the sizes get larger with decreasing N_{co}. In the next section we will evaluate whether this is a consequence of the higher N_H regions being embedded in the lower N_H regions. 2) As the redshift decreases, the median sizes of structures decrease. This effect is not as pronounced at large N_{co} as it is at small N_{co}. Roughly, at $10^{12.5}$ cm^{-2} the median radius of the disk/sphere decreases from 1200/800 kpc at $z = 3$, to 600/400 kpc at $z = 2$, to 300/200 kpc at $z = 1$. At 10^{13} cm^{-2} the median disk/sphere radii are ∼1000/600 kpc ($z = 3$), 500/300 kpc ($z = 2$), and 250/200 kpc ($z = 1$). At the 10^{14} cm^{-2} contour level the median radii are ∼300/200 kpc ($z = 3$), 175/100 kpc ($z = 2$), and 125/100 kpc ($z = 1$). These sizes must be interpreted with caution because accidental coincidences are more likely at high z and they do tend to push upward the size estimates, however they are based on the large sized box where the effect of chance coincidences is

less important. 3) The size constraints increase with increasing DLOS separation. This is likely to be partially due to contamination by chance pairs, but it is also of interest to note that this agrees with the result of Fang *et al.* (1995) in their similar analysis of observational data. They point out that this effect could be a result of a non-uniform size population or of correlated structures. 4) Our size estimates from the numerical simulations (100-300 kpc at $z = 2$ over the N_{co} range 10^{13} — 10^{14} cm^{-2}) are quite consistent with the median of $R = 150$ kpc derived from the observations of Q1343+266 A,B assuming a population of spheres.

3.2. Column Densities for Coincident Lines

In Fig. 1 of CCL95 we presented results of Monte–Carlo simulations that generate the distributions of column densities for pairs of coincident lines in several idealized cases in which Lyα absorption is produced by a single population of identical structures. We considered an irregular distribution of material for which column densities are unrelated to each other, independent of DLOS separation, and we considered spherical and disk structures in which the column density falls off gradually from a central peak. In all cases we assumed that the one population of structures has an N_H distribution consistent with the observed distribution $f(N_H) \sim N_H^{-1.5}$ for the entire population of Lyα forest lines. For "smooth sphere" or "smooth disk" structures this power law $f(N_H)$ results from a column density law $N_H(R) \sim R^{-4}$. In the CCL95 toy models, for a completely irregular distribution there is no correlation between DLOS column densities for any separation $d = D/R$. However, for the smooth structure, Fig. 1 in CCL95 shows highly correlated column densities N_A and N_B for small d, increasing spread as d is increased, and then a tendency to have small N_A for all large N_B (and vice versa) for $d \sim 1$.

Here, in Fig. 4 we show N_A vs. N_B for all coincidences at $z = 2$ in the 3.2Mpc box with $N_H > 10^{12.5}$ cm^{-2}, defined by the $\Delta V_{co} < 50$ km/s criterion. The sequence a–e shows, with increasing D, the increasing spread in the correlation between N_A and N_B. For the large box simulation, the correlation at small D is considerably tighter between N_A and N_B because 12.5 kpc is sub-cell so that A and B are not sampling independent locations. However, it is illustrated in Fig. 4f that the correlation is stronger for the 9.6 Mpc box even when $D = 100$ kpc, and this is likely to be a real effect related to the enhanced large-scale power, since 100 kpc is safely larger than the resolution (~ 25 kpc) at $z = 2$.

The results of Fig. 4 appear very similar to the smooth density distribution toy models in Fig. 1 of CCL95, indicating that such a model is a fairly good description of the numerical simulation results. The spread in this series of plots with increasing D can be used to match them to the toy models, which are expressed in terms of the dimensionless parameter $d = D/R$. Roughly, the $D = 50$ kpc appears most similar to the toy model with $d = 0.1$. This comparison yields an independent estimate of the structure size: $R \sim 500$ kpc at the $10^{12.5}$ cm^{-2} contour level. At the largest D displayed (= 200 kpc, Fig. 4e), the distribution of N_A vs. N_B resembles that for an irregular distribution, with the column densities unrelated between the DLOS. As D is further

increased we do not observe in the simulations the tendency for large N_A values when we have small N_B values, as seen for the toy models. This is not surprising, since at large D many "coincidences" occur just by chance, and since this effect will be washed out by a more realistic distribution of structure sizes and shapes.

For higher column density thresholds, the N_A vs. N_B plots appear qualitatively similar, however the "match" to the toy models occurs for a smaller R value. At $z = 2$, for coincidences with a 10^{13} cm^{-2} threshold, the $D = 50$ kpc figure has scatter consistent with $d \sim 0.25$ in the toy models, yielding $R \sim 200$ kpc. Similarly, for a 10^{14} cm^{-2} threshold we find that $d = 0.5$ corresponds to $D = 50$ kpc so that R is about 100 kpc.

The sizes estimated here are fairly consistent with the Bayesian analysis in the previous section, based on the numbers of coincidences and anticoincidences, certainly within the 90% confidence limits. It is interesting to consider the implications of these results for the density of material within the structures. The consistency with the toy model indicates a smoothly decreasing distribution of mass around density peaks, but not necessarily a single population of separate structures. The sizes estimated in this section relate to the rate of decrease of N_H with R around a density peak. This will be discussed further in the concluding section.

A related DLOS plot is the equivalent width difference between coincident lines in A and B vs. the maximum equivalent width of the two lines. For the $D = 40$ kpc DLOS Q1343+266 A,B at $z \sim 2$, Fang *et al.* (1995) find a trend for high equivalent width lines to have larger equivalent width differences. In the simulations, a series of plots with increasing D would show points moving from the horizontal line with zero equivalent width difference to the correlation line representing the maximum equivalent width difference. Fig. 5 presents the results from the simulation with box size 3.2Mpc at $z = 2$, with $N_{co} = 10^{14}$ cm^{-2} and $\Delta V_{co} = 150$ km/s, the case that should most closely resemble the 1343+266 A,B observations which have an equivalent width cutoff of about 0.3Å. The simulation results appear consistent with the limited data for Q1343+266 A,B observations, but note that the simulations predict a scatter of $|W_A - W_B|$ values at large $\max(W_A, W_B)$ that would only become apparent in a larger observed sample.

Finally, the N_A vs. N_B plots provide another way of considering the level of contamination by chance coincidences. These chance coincidences should be distributed in the N_A vs. N_B diagram as an irregular toy model distribution would be, or equivalently as a distribution with a very large D value such as in Fig. 4e. If these chance pairs are a dominant contributor to the total number of coincidences we should see a significant scatter from the correlation lines. We see some outlying points, in Figs. 4a and 4b for example, that could be due to chance pairs, but this is not a significant effect. Such contamination is observed to be more pronounced at $z = 3$ (and less pronounced in the 9.6 Mpc box simulations), but it is significant that a correlation between N_A and N_B is still quite apparent at $D = 100$ kpc even in the $z = 3$ simulation results.

3.3. Velocity Differences for Coincident Lines

Next, we examine the distribution of velocity differences between coincident lines for the various DLOS separations. Figs. 6a, b, and c show (for $z = 3$, 2, and 1) the distributions for all coincident lines with $N_{co} = 10^{12.5}$ cm^{-2} in the small 3.2 Mpc box, chosen for its high resolution at small D separations. We display all the data up to $\Delta V = 150$ km/s, but many of the contributing pairs at $\Delta V > 50$ km/s are chance coincidences (as discussed above) so we should focus on comparisons at small ΔV. These distributions are normalized so that $f(\Delta V) = 1$ at 5 km/s (the center of the first bin). The results are nearly identical in the 9.6 Mpc simulations. For very small D nearly all coincident lines have $\Delta V < 10$ km/s, and the distribution gradually widens with increasing D. There is an apparent difference between the distributions at the three different redshifts for a fixed D value, but in interpreting this trend we must again consider the effect of contamination by chance pairs. At $D = 800$ kpc the $f(\Delta V)$ distributions for coincident pairs are nearly identical to those derived from chance coincidences in the "control" sample (filled circles). These large D/control sample distributions would be flat except for the omission of adjacent lines from the coincident sample, an effect that is most significant at large redshifts. At $z = 1$ where chance coincidences have a minor contribution, the $D = 800$ kpc case is nearly flat. At large D where the contribution of chance coincidences is significant, the evolution of the width of the $f(\Delta V)$ distribution from $z = 3$ to $z = 1$ has a large contribution from contamination, and is therefore difficult to interpret. For smaller D, the effect of contamination (see Fig. 4) is small, as evidenced by the narrow ΔV distribution.

The sets of velocity distribution curves in Fig. 6 closely resemble those expected for a disk with systematic motion, either rotation or inflow/outflow in the plane (see Fig. 3 in CCL95). If we use the comparison to estimate d values, as we did in the previous section for the N_A vs. N_B curves, we obtain similar results. For example, at $z = 2$ the curve with $D = 200$ kpc approximately matches the $d = 0.5$ curve for a disk with inflow/outflow velocity of ~ 100 km/s, yielding $R \sim 400$ kpc for the $10^{12.5}$ cm^{-2} contounr level. In CCL95, we noted a difference expected between rotation and inflow/outflow in a plane, with a predicted decrease in ΔV distribution width for $d > 1$ in the case of inflow/outflow. Such a trend would be difficult to recognize here due to the uncertainties of chance coincidence contributions.

The ΔV distribution can be compared at the different redshifts if the curves are labeled by their appropriate values of d. For Figs. 6a, b, and c the $D = 800$ kpc curves correspond to $d = 1$, 2, and 4, respectively. With this rescaling, the velocity distributions for a given d are narrower at lower redshifts. For coincident pairs with the larger column density cutoffs, N_{co}, we find that the ΔV distributions are wider at a given D. This is shown for $N_{co} = 10^{14}$ cm^{-2} at $z = 3$ in Fig. 6d. However, if the curves are labeled with estimates of the appropriate values of $d = D/R$ from Fig. 3 then the series of curves are similar for the different N_{co} values. The shapes of these histograms are consistent with models of rotating disks or of inflow/outflow in a sheet. If this type of systematic motion is responsible, then a narrowing of the distribution with time would represent a decrease in the rotation or inflow/outflow velocity.

3.4. Anticoincident Column Density Distributions

The anticoincident column density distribution was considered in CCL95 as a method to distinguish between spherical and disk geometries. For a smoothly falling density profile in a sphere, small D DLOS should always yield relatively small values of the anticoincident column density, while for a disk of arbitrary orientation it is possible to obtain a larger value. As the DLOS separation is increased, we expect to obtain the distribution $f(N_{ac}) \sim N_{ac}^{-1.5}$. The number of anticoincidences is decreased by the presence of chance coincidences, but there should be no bias with N_H, i.e. the remaining anticoincidences should have the same $f(N_H)$ as the true full distribution.

In Fig. 7, the anticoincident column density distributions are presented for $N_{co} = 10^{12.5}$ cm^{-2} and $\Delta V_{co} = 50$ km/s and for $N_{co} = 10^{14}$ cm^{-2} and $\Delta V_{co} = 150$ km/s (for the 3.2 Mpc box simulations at $z = 3$, 2, and 1). Again, the simulation curves resemble the expectations for a smooth column density profile (eg. with $N_H(R) \sim R^{-4}$ as in the CCL95 toy models) but are inconsistent with a spherical geometry. For a DLOS with $d < 0.25$ through a sphere with a sharp edge, there should not be any anticoincidences with N_{ac} more than three times the cutoff value. For $N_{co} = 10^{12.5}$ cm^{-2} at $z = 2$, all curves with $D < 200$ kpc must have $d < 0.25$ (using our previous size estimates) and we see many anticoincidences with large N_{ac} values. However, all series of curves do show an excess of small N_{ac} values (relative to large ones) for close DLOS separations, similar to the expectations for the disk geometry. In this geometry the large N_{ac} values arise from LOS that pass close to the center of a disk that is highly enough inclined that the other LOS falls beyond the edge. For $N_{co} = 10^{14}$ cm^{-2}, the smallest D value of 12.5 kpc corresponds to $d \sim 0.05$ – 0.12 over the range of redshifts, $z = 3$ to $z = 1$. The deficit of large column densities, i.e. the steepening of the slope at small N_{ac} of the curves with small d values, is significant: for the total number of anti–coincidences in the simulations (thousands even for $D = 12.5$ kpc) these results are not affected by small number statistics.

We conclude that there is a tendency for anticoincidences for very small DLOS separations to be biased toward small column densities, i.e. it is not as common to find a *much* larger column density along a LOS close to another LOS for which $N_H < N_{co}$. However, the fact that relatively large column densities *are* occasionally observed close to an anticoincident LOS implies the simulations are not composed of spherical structures with sharp edges. Rather, the results are again consistent with flattened structures with a relatively smooth density profile, since some of these can be oriented so that two LOS separated by small D can have drastically different column densities.

4. Summary and Discussion

We have analysed data from two cosmological N–body/hydrodynamic simulations (with box sizes 3.2 Mpc and 9.6 Mpc) to study the formation and evolution of the Lyα forest in a flat CDM dominated universe. Synthetic spectra were generated at $z = 3$, 2, and 1 to mimic the observations of double quasar lines of sight, and analyzed with various tests developed to study DLOS as if they

were observational data.

We find that a DLOS analysis of the numerical simulations yields results very similar to those obtained from idealized models in which Lyα *absorption is produced by a single population of disks with* $N_H(R) \sim R^{-4}$ (CCL95). In particular: 1) Lines coincident in both lines of sight exhibit an increasing spread of column densities from the correlation line as the DLOS separation is increased (Fig. 4). 2) The velocity difference distribution for coincident lines gets wider for more widely spaced DLOS (Fig. 6), as expected for coherent motion in the plane of a disk. This behavior is also expected for pure Hubble flow, and with this diagram alone we cannot distinguish the two. 3) The distribution of column densities for anticoincidences does exhibit some large values for DLOS with all separations, though at small D there are a smaller fraction of large values than in the sample of all Lyα lines, i.e. than in the $f(N_H) \sim N_H^{-1.5}$ distribution (Fig. 7). This indicates that spherical clouds are not a good description of the simulation data. 4) A Bayesian estimate of structure sizes based on the observed numbers of coincidences and anticoincidences yields larger sizes for lower N_H contour levels (Fig. 3), as would result from a density distribution that decreases smoothly from a central value.

Although the DLOS analysis of the simulation data is generally suggestive of absorption arising from a population of similarly sized structures, with smoothly declining density profiles from a central maximum, some aspects of the analysis show that this is a simplification. The Bayesian analysis of structure size yielded a size that increases with the DLOS separation used to probe it. Interestingly, the same result was obtained from analysis of observational data at several different separations by Fang *et al.* (1995) who find it to be consistent with some models of different size distributions and/or clustering of somewhat smaller absorbing structures. Our DLOS analysis of simulation data adds the additional constraint that a correlation between the column densities of DLOS must hold out to fairly large D, thus there must be fairly large individual structures involved.

The size of structures at fixed column densities is found to decrease with decreasing redshift in the simulation data, although this could be partly due to the effects of contamination by chance pairs and the increased line densities at high redshifts. Roughly, we find that derived sizes for structures defined by the $N_{co} = 10^{12.5}$ cm^{-2} contour level decrease from $\sim$1000 kpc to a couple hundred kpc from $z = 3$ to $z = 1$, while at the $N_{co} = 10^{14}$ cm^{-2} level they decrease from a couple of hundred kpc to about 100 kpc in radius. These constraints are quite consistent with the median radius of 149h^{-1} kpc at $N_{co} \sim 10^{13.5}$ cm^{-2} and $z = 1.8$ derived from observations of DLOS Q1343+2640 A,B (Dinshaw *et al.* 1994, Bechtold 1994, Fang *et al.* 1996). When scaled by the structure size (i.e. at a fixed value of D/R, the ratio of the DLOS separation to the structure radius), the internal structure and motion of the Lyα absorbers, as diagnosed by DLOS analysis, is similar at different redshifts and N_H contour levels.

All of the conclusions that we have reached are subject to an uncertainty, which will also affect future DLOS observations more than it has in the past. As the column density threshold for detecting lines is decreased, and as the redshift is increased, the probability of detecting "coincidences"

for completely unrelated lines of sight will increase. This effect tends in the direction of biasing estimates toward larger sizes for high redshifts and small N_H. It is simple enough to correct for the problem in the case where a few such accidental coincidences are expected, but in the case where the probability of such a false coincidence approaches unity for each line (as for $N_{co} = 10^{12.5}$ cm^{-2} and $z = 3$) the situation is more confused. In view of the fact that 8–m class telescopes will push DLOS detection thresholds to considerably lower levels ($N_{co} \sim 10^{12.5}$ cm^{-2}), new techniques must be developed to understand the problems associated with random superpositions of unrelated lines.

This DLOS analysis of the numerical simulation data yields results consistent with similar analyses of the much smaller amount of observational data available thus far (Charlton, Churchill, & Linder 1995, Fang *et al.* 1996). If this were an analysis of real observed spectra then we would have to accept at face value the inference that absorption arises from flattened structures with N_H that fall smoothly from peak values and with coherent velocity structure. However, the numerical simulation laboratory allows us to check these conclusions, and to examine in more detail the nature of the internal structure and motion.

Regarding the distribution of material responsible for absorption, we would like to check and see if a typical structure really does show a decrease of column density with radius in the way that our idealized single population models would require, i.e. $N(R) \sim R^{-4}$. The following questions are also of interest: To what extent are the structures disk-shaped? Are they individual structures or are they interconnected on a larger scale? What fraction of the absorption at a given contour level is produced in "smooth" density law structures? How uniform in size are structures at various N_H contour levels?

To qualitatively address these points, we display in Fig. 8 contour diagrams for a slice one cell thick through the 3.2 Mpc box at redshifts 3, 2, and 1 (from left to right). The top row sequence shows surface levels of neutral Hydrogen column densities N_H across the single projected cell. The second row of figures shows the same evolution sequence but for the divergence of the peculiar gas velocity. In each case, the slice is chosen to intersect the densest structure in the box.

The structures responsible for absorption can extend through more than a single cell. In fact, at $z = 3$ contours of $N_H = 10^{12.5}$ cm^{-2} appear as an extended and interconnected system of sheet–like structures that surround regions of higher density. (However, we emphasize that the column densities quoted here are integrations across only a single cell and are thus likely to be much lower than those computed from the DLOS integrations across the whole of these structures.) Higher contour levels (10^{13} cm^{-2}) define more compact but elongated structures such as filaments. Still higher column density contours ($> 10^{14}$ cm^{-2}) define spherical knots or halos and are typically found at the intersections of filaments. At lower redshifts, the mean density throughout the box decreases with the expansion of the universe and the $10^{12.5}$ cm^{-2} contours are no longer simply connected in sheet–like structures, but are more likely to surround higher density regions such as filaments. They are much less extended, while the higher density contours are less noticeably different in size. The sheet–like structures are still present but are now identified with lower column

densities $\sim 10^{11}$ cm^{-2}. Results from the Bayesian analysis of structure sizes as a function of redshift are consistent with the picture presented here. The lower density thresholds, which define extended structures at high redshifts, correspond to more compact objects as the universe expands to smaller redshifts, and structures at the same threshold thus appear to decrease in size. The higher density structures are less sensitive to this effect as they are compact to begin with, and their evolution in size is not as pronounced. It is of interest to note that the decreasing structure size noted in these simulations is opposite to the conclusion from DLOS size analysis of observational data (Fang *et al.* 1996). However, the only available low redshift DLOS ($z \sim 0.7$) has a large separation ($D \sim 330\mathrm{h}^{-1}$ kpc) and we have seen in Fig. sizes that size estimates based on large D DLOS are inflated.

Figure 8 also provides a direct estimate for the size of structures. For example, at $z = 2$, the filamentary structures appear to have a coherence length ranging from a few hundred kpc up to about 1 Mpc, with a thickness of 100 — 200 kpc. The higher density spherical structures have typical radii up to a few hundred kpc. This is again consistent with the DLOS analysis. We also note that by computing the density field around the spherical structures we can test the hypothesis that $N_H(R) \sim R^{-\alpha}$, with $\alpha = 4$, is roughly correct in describing the distribution of column densities. We have done this experiment by integrating the densities along 1/4 of the box size in the z direction, centered on the highest density peak. The resulting two-dimensional grid of column densities are then averaged and binned into a spherical distribution, centered on the peak. We find that in the central most regions $R \leq 10$ kpc the distribution varies as a power law with index $\alpha \sim 4$, steepens significantly to a maximum $\alpha \sim 9$ at the intermediate radius $R \sim 50$ kpc, then becomes shallower again with $\alpha \sim 3$ at $R \sim 200$ kpc. An averaged effective index over this entire domain is roughly consistent with the distribution $N_H(R) \sim R^{-4}$.

The velocity structure in the absorbers can be understood by examining the contour map of the local divergence in the peculiar velocity flow (the redshift sequence along the second row in Fig. 8). This map shows that the gas around the high density contours is generally falling in towards the central core regions, due to gravitational and cooling instabilities. This is evidenced by the negative velocity divergence which is correlated nicely with the high density spherical structures found in the N_H contours. There is also a component of velocity, due mostly to gravity, that is responsible for the merging of coherent matter distributions within the larger sheet–like structures. In the low density regions or voids, the velocity divergence is mostly positive, suggesting that material is moving away from the the centers of the voids towards the higher density filaments. Although the flow is complex, it appears there is coherent motion in the structures that is consistent with the diagnosis of the DLOS analysis.

Basically, the DLOS analysis of numerical simulation data, although incomplete, yielded fairly reliable insights into the nature of the structure responsible for Lyα absorption. Further information can be extracted from more detailed examination of the three-dimensional maps in position and velocity afforded by the simulations. Double line of sight analysis of future observational data will not yield this level of detail, but it should be possible to utilize the tests developed here to recognize

the basic nature of the observed structure.

We acknowledge support from NASA grant NAGW–3571 at Penn State, NSF grant ASC–9318185 (funding the Grand Challenge Cosmology Consortium GC^3) and PSC grant AST950004P at NCSA. The simulations and data analysis were performed on the Convex-3880 and the Convex Exemplar at the National Center for Supercomputing Applications, University of Illinois at Urbana-Champaign, and the Cray C90 at the Pittsburgh Supercomputing Center.

REFERENCES

Anninos, P., Norman, M. L., and Clarke, D. A. 1994, ApJ, 436, 11

Anninos, P., Zhang, Y., Abel, T., and Norman, M. L. 1996, in preparation

Bahcall, J. N. *et al.* 1996, ApJ, in press

Bechtold, J. & Yee, H. K. C. 1996, ApJ, in press

Bechtold, J. 1994, ApJS, 91, 1

Bechtold, J., Crotts, A. P. S., Duncan, R. C., & Fang, Y. 1994, ApJ, 437, L83

Bi, H., Ge, J., & Fang, L.Z. 1995, preprint

Cen, R., Miralda–Escudé, J., Ostriker, J.P. and Rauch, M. 1994, ApJ, 437, L9

Charlton, J. C., Churchill, C. W., and Linder, S. M. 1995, ApJ, 452, L81 (CCL95)

Dinshaw, N., Foltz, C.B., Impey, C.D., Weymann, R.J., and Morris, S. L. 1995, Nature, 373, 223

Dinshaw, N., Impey, C.D., Foltz, C.B., Weymann, R.J., and Chaffee, F. H. 1994, ApJ, 437, L87

Fang, Y., Dunca, R. C., Crotts, A. P. S., & Bechtold, J. 1996, ApJ, submitted

Hernquist, L., Katz, N., Weinberg, D. H., Miralda–Escudé, J. 1996, ApJ, submitted

Ikeuchi, S., & Ostriker, J. P 1986, ApJ, 301, 522

Lanzetta, K. M., Bowen, D. V., Tytler, D., & Webb, J. K. 1995, ApJ, 442, 538

Lu, L., Wolfe, A. M., and Turnshek, D. A. 1991, ApJ, 367, 19

Miralda–Escudé, J., Cen, R., Ostriker, J. P, and Rauch, M. 1996, ApJ, submitted

Miralda–Escudé, J., Rees, M.J. 1993, MNRAS, 260, 617

Rees, M.J. 1986, MNRAS, 218, 25

Sargent, W. L. W., Young, P., Boksenberg, A., & Tytler, D. 1980, ApJS, 42, 41

Smette, A., Surdej, J., Shaver, P.A., Foltz, C.B., Chaffee, F.H., Weymann, R.J., Williams, R.E., and Magain, P. 1992, ApJ, 389, 39

Smette, A., Robertson, J. G., Shaver, P. A., Reimers, D., Wisotzki, L., & Kohler, Th. 1995, å, in press

Spitzer, L. *Physical Processes in the Interstellar Medium*, (John Wiley & Sons, 1978)

Zhang, Y., Anninos, P., & Norman, M. L. 1995, ApJ, 453, L57

Zhang, Y., Anninos, P., & Norman, M. L. 1996, ApJ, in preparation

This preprint was prepared with the AAS LaTeX macros v4.0.

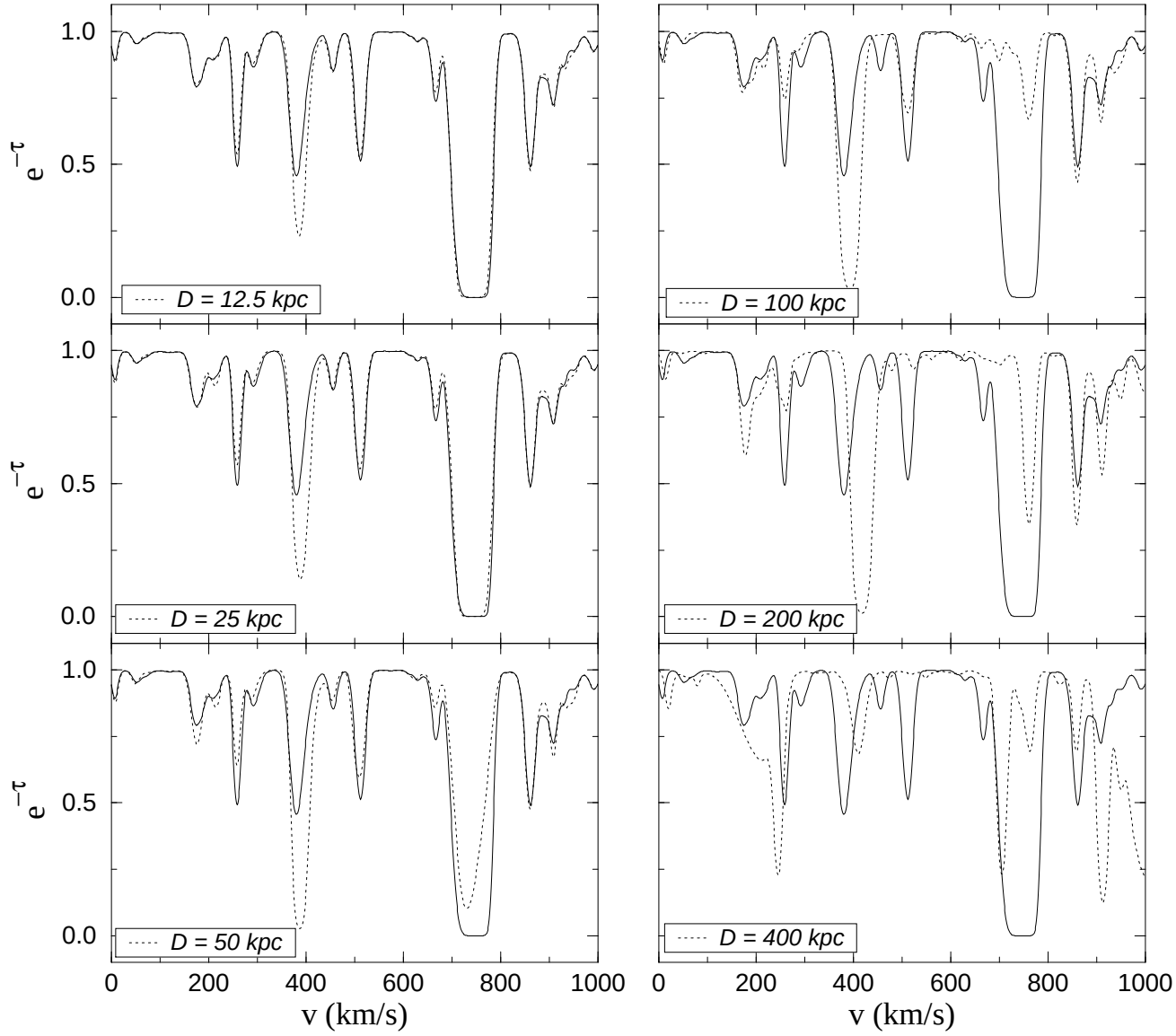

Fig. 1.— The solid lines show the transmission along the same line of sight through the 3.2 Mpc box simulation at $z = 2$. The dotted lines in each graph represent different parallel lines of sight separated by a distance D.

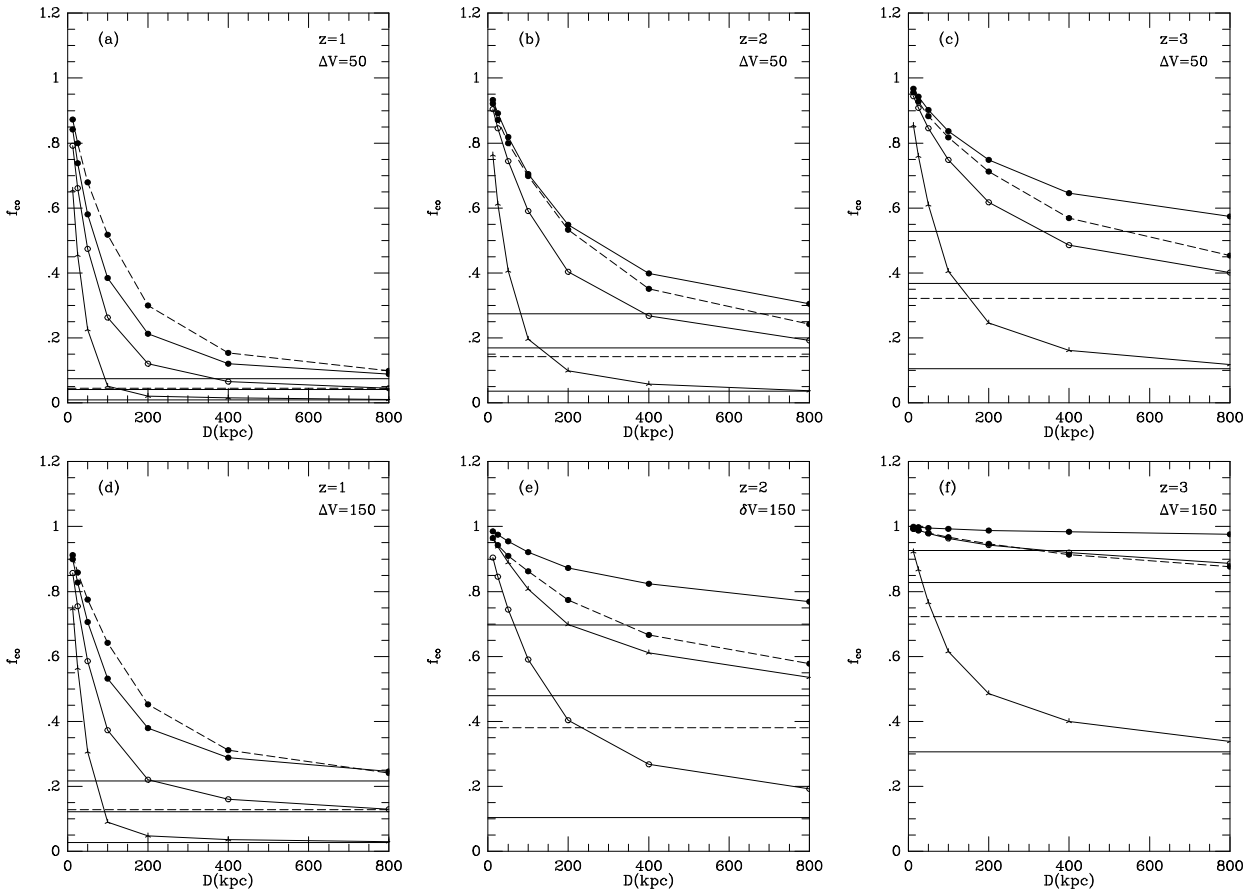

Fig. 2.— The ratio of the number of coincidences to the number of coincidences plus anticoincidences, f_{co}, as a function of the DLOS separation, D. In determining this fraction, lines classified as adjacent (within ΔV_{co} but not the nearest line) are disregarded both in the numerator and in the denominator. The three solid curves in each part are drawn for $N_{co} = 10^{12.5}$, 10^{13}, and 10^{14} cm^{-2}, from top to bottom. The three solid horizontal lines represent the expected f_{co} for completely unrelated lines of sight (determined by splitting each single LOS into two parts and analyzing them as a DLOS) for the same three N_{co}. All solid lines in this figure are determined from the 3.2 Mpc box simulation. For comparison, the dashed curves give f_{co} for the $N_{co} = 10^{12.5}$ cm^{-2} cutoff in the 9.6 Mpc box simulation, and the dotted lines are the corresponding expected fraction of chance coincidences. — (a) $z = 1$, $\Delta V_{co} = 50$ cm^{-2}, — (b) $z = 2$, $\Delta V_{co} = 50$ cm^{-2}, — (c) $z = 3$, $\Delta V_{co} = 50$ cm^{-2}, — (d) $z = 1$, $\Delta V_{co} = 150$ cm^{-2}, — (e) $z = 2$, $\Delta V_{co} = 150$ cm^{-2}, — (f) $z = 3$, $\Delta V_{co} = 150$ cm^{-2}.

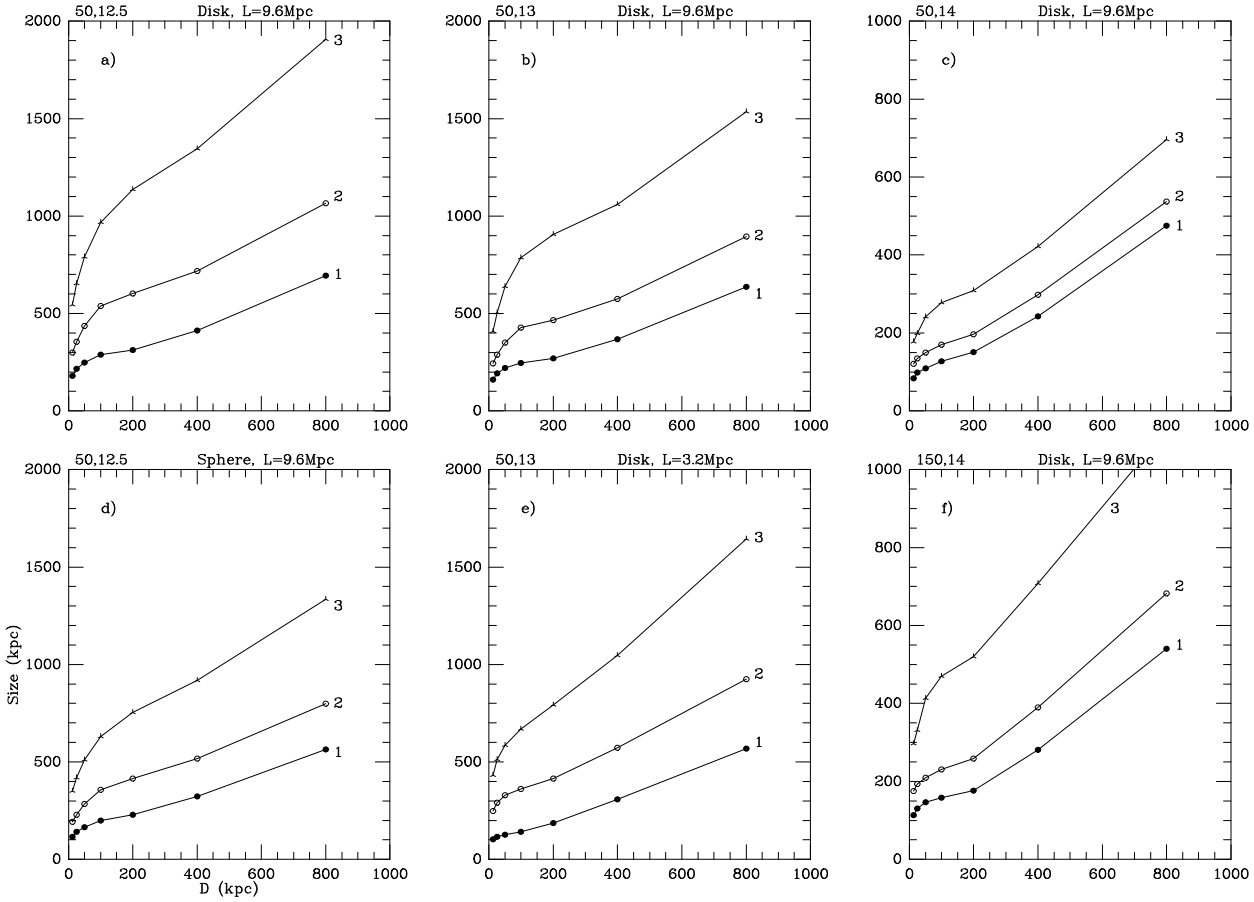

Fig. 3.— The median sizes from the probability distribution derived from Bayesian analysis of the number of coincidences and anticoincidences. Sizes are calculated from DLOS with separations 12.5, 25, 50, 100, 200, 400, and 800 kpc, for the assumption of a single size population of spheres or of disks. The three curves represent, from top to bottom, redshifts 3, 2, and 1. For each series the box-size, geometry, neutral column density contour level N_{co}, and velocity criterion for a coincidence ΔV_{co} are: — (a) 9.6 Mpc box, disk, $N_{co} = 10^{12.5}$ cm^{-2}, $\Delta V_{co} = 50$ km/s, — (b) 9.6 Mpc box, disk, $N_{co} = 10^{13}$ cm^{-2}, $\Delta V_{co} = 50$ km/s, — (c) 9.6 Mpc box, disk, $N_{co} = 10^{14}$ cm^{-2}, $\Delta V_{co} = 50$ km/s, — (d) 9.6 Mpc box, sphere, $N_{co} = 10^{12.5}$ cm^{-2}, $\Delta V_{co} = 50$ km/s, — (e) 3.2 Mpc box, disk, $N_{co} = 10^{13}$ cm^{-2}, $\Delta V_{co} = 50$ km/s, — (f) 9.6 Mpc box, disk, $N_{co} = 10^{14}$ cm^{-2}, $\Delta V_{co} = 150$ km/s.

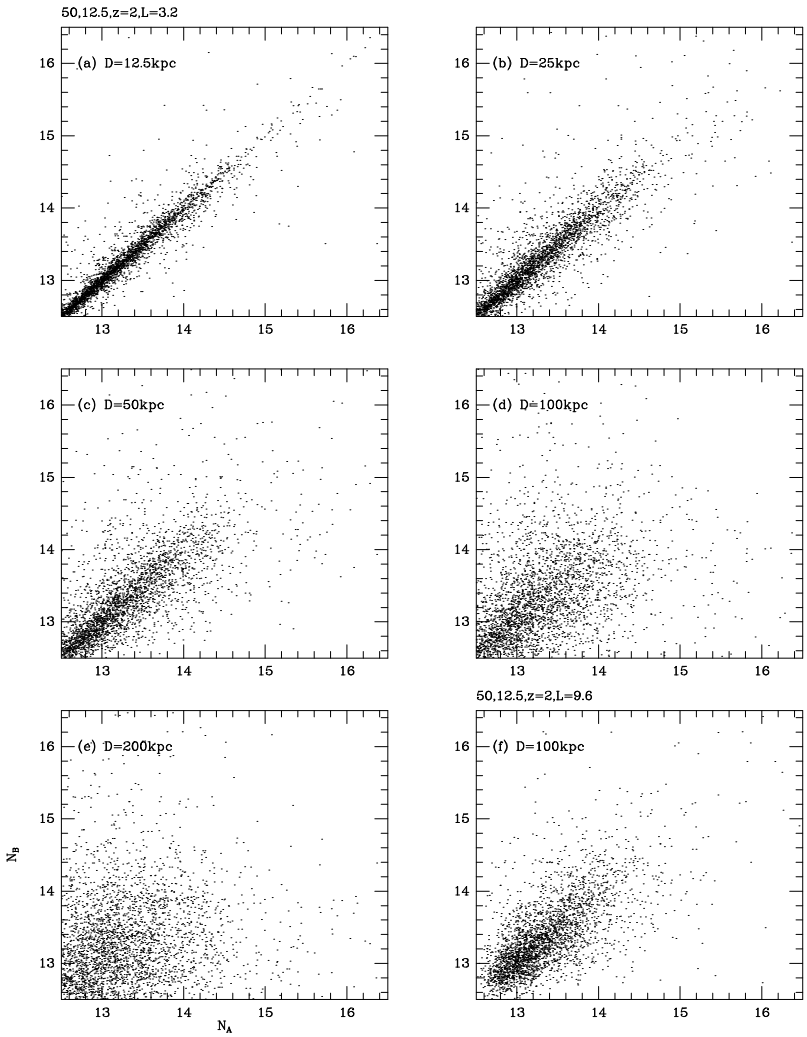

Fig. 4.— Neutral column densities for pairs of coincident lines along double lines of sight, N_A vs. N_B, for various DLOS separations. For clarity only 3000 points are plotted on each diagram. — (a) – (e) Series with increasing DLOS separation for coincidences with $N_{co} = 10^{12.5}$ cm^{-2} and $\Delta V_{co} = 50$ km/s at $z = 2$ in the small (3.2 Mpc) box. — (f) $D = 100$ kpc separation DLOS at $z = 2$, the same as in part (d) except for the large (9.6 Mpc) box.

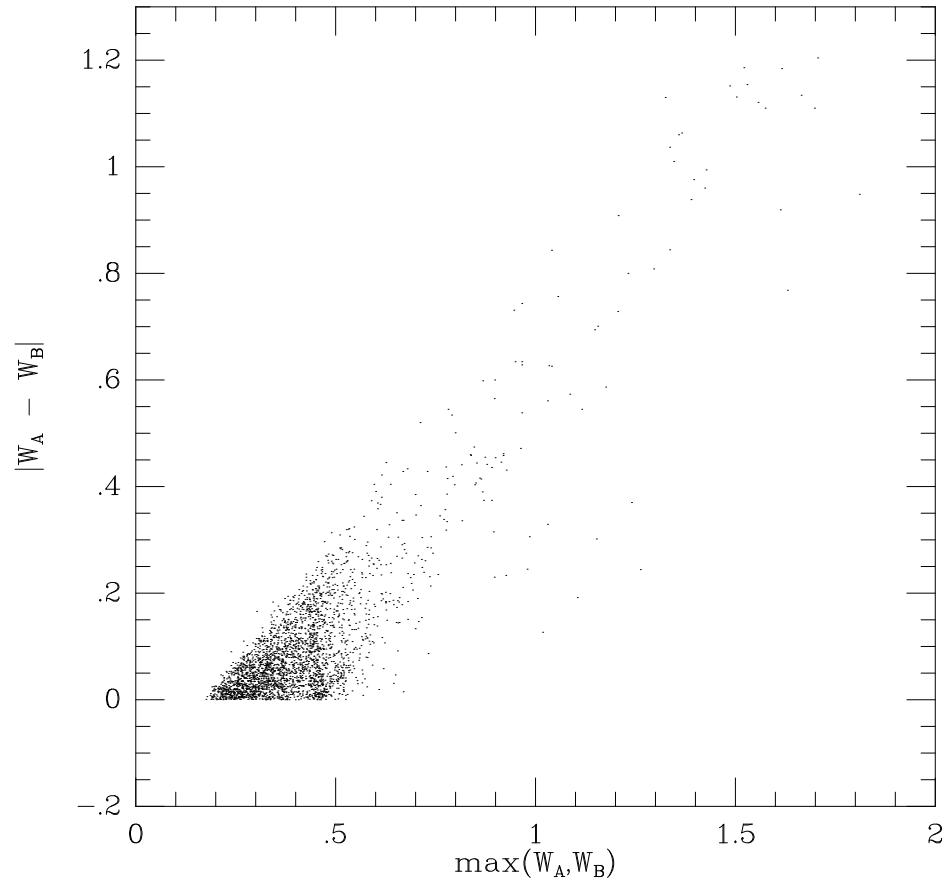

Fig. 5.— The absolute value of the equivalent width difference for the two members of a coincident pair vs. the maximum value of equivalent width for a member of that pair. To facilitate comparison with the observed DLOS Q1343+2640 A,B, coincidences are displayed for $D = 50$ kpc at $z = 2$ for the cutoff values $\Delta V_{co} = 150$ km/s and $N_{co} = 10^{14}$ cm^{-2} for the 3.2 Mpc box simulation. Only 3000 points are plotted.

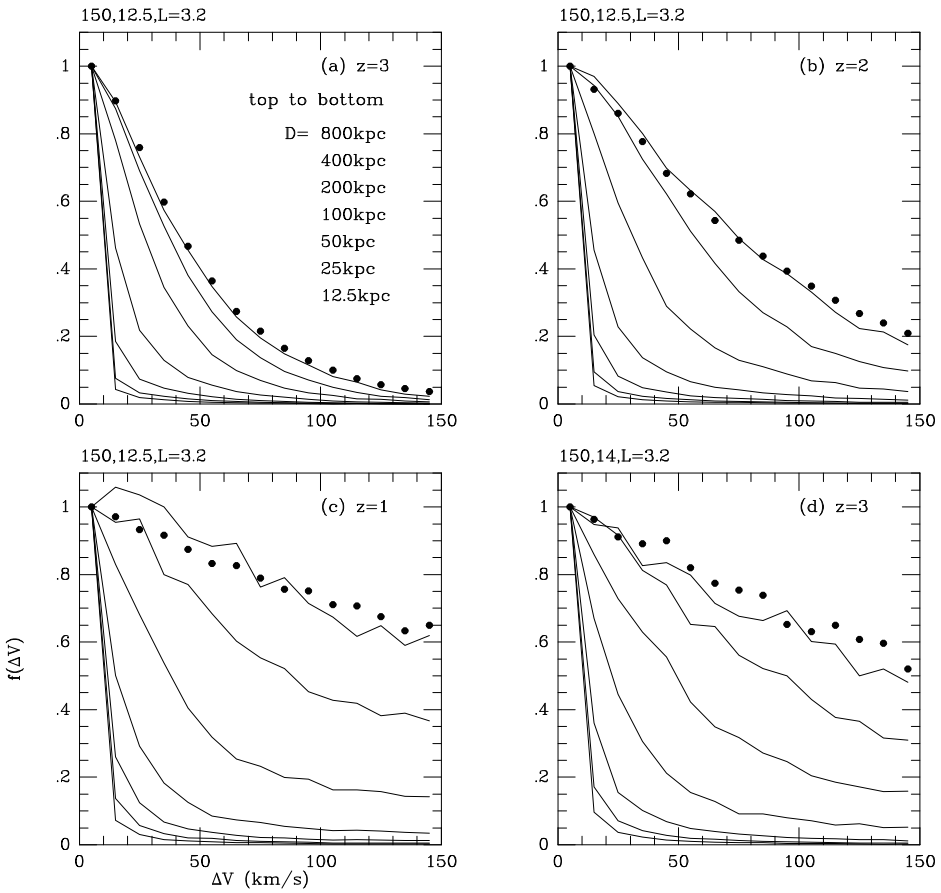

Fig. 6.— Distribution of the differences in line of sight velocity between members of coincident pairs. The series of curves covers DLOS with separations 12.5, 25, 50, 100, 200, 400, and 800 kpc, from bottom to top. All results are for the 3.2 Mpc box simulations, and are normalized to $f(\Delta V) = 1$ for the point in the smallest bin at 5 km/s. Points represent the distribution of ΔV for the chance coincidences derived from unrelated LOS at the given redshift and cutoff values. — (a) $z = 3$, $N_{co} = 10^{12.5}$ cm^{-2}, $\Delta V_{co} = 150$ km/s, — (b) $z = 2$, $N_{co} = 10^{12.5}$ cm^{-2}, $\Delta V_{co} = 150$ km/s, — (c) $z = 1$, $N_{co} = 10^{12.5}$ cm^{-2}, $\Delta V_{co} = 150$ km/s, — (d) $z = 3$, $N_{co} = 10^{14}$ cm^{-2}, $\Delta V_{co} = 150$ km/s,

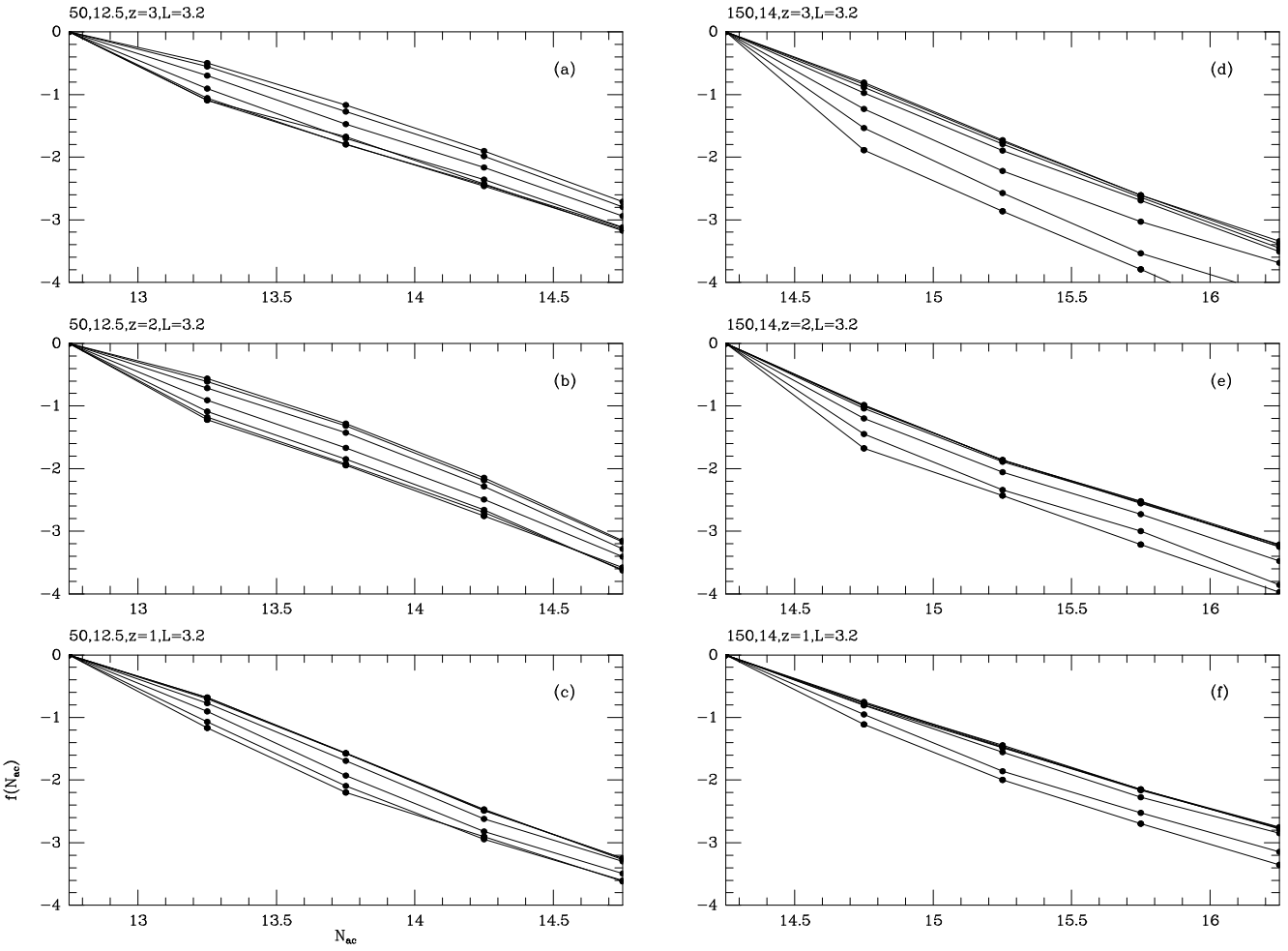

Fig. 7.— Distribution of neutral column densities for anticoincident lines are given for various DLOS separations (12.5, 25, 50, 100, 200, 400, and 800 kpc from bottom to top) in each plot. All cases displayed are for the $L = 3.2$Mpc box. — (a) $N_{co} = 10^{12.5}$, $\Delta V_{co} = 50$ km/s, $z = 3$, — (b) $N_{co} = 10^{12.5}$, $\Delta V_{co} = 50$ km/s, $z = 2$, — (c) $N_{co} = 10^{12.5}$, $\Delta V_{co} = 50$ km/s, $z = 1$, — (d) $N_{co} = 10^{14}$, $\Delta V_{co} = 150$ km/s, $z = 3$, — (e) $N_{co} = 10^{14}$, $\Delta V_{co} = 150$ km/s, $z = 2$ — (f) $N_{co} = 10^{14}$, $\Delta V_{co} = 150$ km/s, $z = 1$

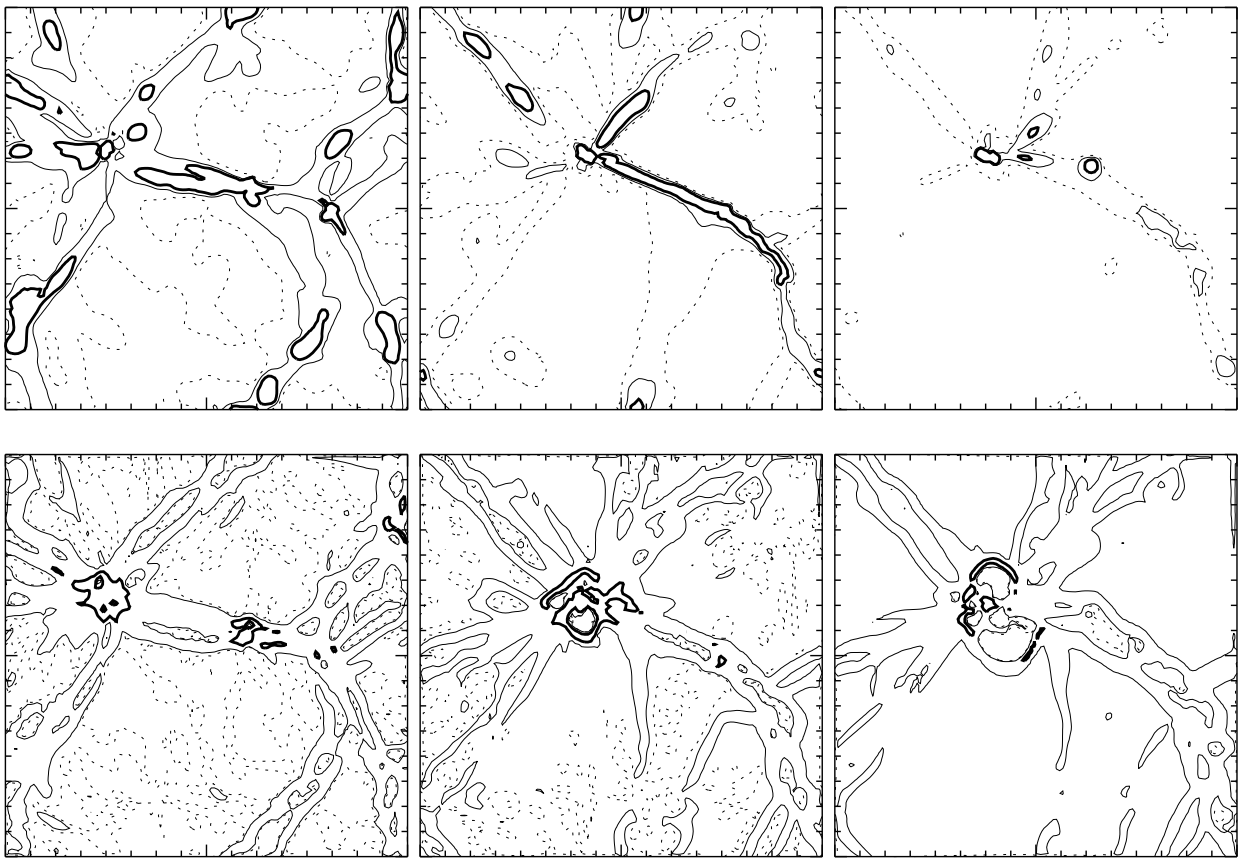

Fig. 8.— First Row: Surface plot of a single slice in the 3.2 Mpc box showing the neutral hydrogen column density N_H for $z = 3$, 2, and 1 (left to right). Three contour levels are shown: 10^{11} cm^{-2} (dotted lines), 10^{12} cm^{-2} (solid lines) and 10^{13} cm^{-2} (thick solid lines). Second Row: Surface plots showing the divergence of the baryonic peculiar velocity field. The box size, redshifts and slices are the same as those in the N_H contours above. Three contour levels are shown: -50 (thick solid lines), 0 (solid lines) and $+5$ (dotted lines) in units of the inverse Hubble time $hH_0^{-1} = 3.1 \times 10^{17}$ sec.